


Cite this: *Nanoscale Adv.*, 2019, 1, 4669

Received 20th August 2019  
Accepted 12th October 2019

DOI: 10.1039/c9na00521h

rsc.li/nanoscale-advances

# Engineering doping-vacancy double defects and insights into the conversion mechanisms of an Mn–O–F ultrafine nanowire anode for enhanced Li/Na-ion storage and hybrid capacitors†

Yongfa Huang, Rui Ding, \* Danfeng Ying, Wei Shi, Yuxi Huang, Caini Tan, Xiujuan Sun, Ping Gao and Enhui Liu

The behavior of Li/Na-ion capacitors (LICs/NICs) is largely limited by the low number of electroactive sites in conventional insertion-type anodes. In this work, we demonstrated a novel doping-vacancy double-defective and conversion-type Mn–O–F ultrafine nanowire (denoted as MnF<sub>2</sub>-E) anode to boost the number of electroactive sites for enhanced LICs/NICs. Owing to the unique hetero oxygen-doping and intrinsic fluorine-vacancy double defects, the Mn–O–F nanowires exhibited superior electroactive sites and thus dramatically enhanced Li/Na-ion storage capability than pristine MnF<sub>2</sub> micro/nanocrystals. Both the optimal MnF<sub>2</sub> screened by orthogonal experiments and derived Mn–O–F anodes and commercial activated carbon (AC) cathode were used to construct MnF<sub>2</sub>//AC and MnF<sub>2</sub>-E//AC LICs/NICs, which were optimized by tuning the active mass ratios of the cathode/anode and the working voltage windows of the hybrid capacitors. The LICs/NICs based on the Mn–O–F anode demonstrated a considerably superior performance than the devices based on the MnF<sub>2</sub> anode under the optimal voltages of 0–4 V and 0–4.3 V. The Mn–O–F anode exhibited dominant diffusion/surface-controlled kinetics for Li/Na-ion storage, respectively, showing a major conversion mechanism for the charge storage processes. This work provides a new concept of double-defective and conversion-type electrode materials to improve the Li/Na-ion storage capability and will have a significant impact on the relevant fields.

## Introduction

Energy is increasingly inseparable from human life with the development of society; however, the disadvantages of the depletion of fossil fuel resources and environmental pollution limit their applications. Thus, electrochemical energy storage has become one of the most important strategies to solve these

issues.<sup>1</sup> Electrochemical energy storage, which is necessary for future large-scale power grids, is sustainable, green and responsive and can be used in electrochemical engines and smart devices.<sup>2</sup> Electrochemical capacitors (ECs) or supercapacitors (SCs) as an important part of electrochemical energy storage have attracted wide interest from researchers,<sup>3</sup> especially lithium-ion capacitors (LICs)<sup>4,5</sup> and sodium-ion capacitors (NICs).<sup>6,7</sup> Furthermore, non-aqueous hybrid ion capacitors<sup>8,9</sup> usually show a higher working voltage, larger energy density and wider temperature scope than aqueous hybrid ion capacitors.<sup>10</sup>

LIC was proposed by Amatuelli's team in 2001.<sup>11,12</sup> It uses a battery-type material as the negative electrode with high energy density and an electric double layer (EDL) carbon material as the positive electrode with high power density; thus, LICs can export high energy and power density simultaneously. However, the performance of LICs is largely limited by anode materials, which have low electrochemical activity. Thus, finding new anodes with high electroactive sites has become an important research direction. Various advanced materials such as Nb<sub>2</sub>O<sub>5</sub>,<sup>13</sup> MnO,<sup>14</sup> and BiVO<sub>4</sub><sup>15</sup> have been reported as intriguing anodes for LICs.

Nowadays, the depletion of lithium resources has caused widespread concern and more seriously, the development of lithium resources cannot keep up with the development of lithium-ion energy storage devices.<sup>16</sup> Therefore, it is very important to find electrochemical energy storage devices with low cost, high safety, high energy/power densities and long cycle stability. It is particularly attractive to develop other ion energy storage devices for this purpose. Sodium (Na) ions are highly abundant and low cost in nature and have received great attention from researchers as alternatives to lithium ions.<sup>17</sup> Sodium ion capacitors (NICs) also have the advantages of sodium ion batteries of high energy density and EDL capacitors of high power density. Some NICs even exhibit the same performance as LICs, such as Nb<sub>2</sub>O<sub>5</sub>@C/reduced graphene oxide (rGO),<sup>18</sup> TiO<sub>2</sub>/C,<sup>19</sup> N-TiO<sub>2</sub>,<sup>20</sup> 3D framework carbon (3DFC),<sup>21</sup> peanut skin-derived carbon nanosheets-A (SCN-A).<sup>22</sup>

Key Laboratory of Environmentally Friendly Chemistry and Applications of Ministry of Education, College of Chemistry, Xiangtan University, Xiangtan, Hunan 411105, P. R. China. E-mail: drm8122@163.com; drm8122@xtu.edu.cn

† Electronic supplementary information (ESI) available. See DOI: 10.1039/c9na00521h



Electrode materials play a key role in electrochemical energy storage. The choice of materials should be based specifically on the following reasons: firstly, high specific surface area can afford rich electroactive sites, which can ensure high specific capacity. Secondly, high porosity can provide facile pathways for ion transportation and superior endurance for volume change, which can ensure high rate capability and stability. Thirdly, special morphologies such as nanowires and nanotubes, can facilitate the electron/ion transfer rates, which can further enhance the electrochemical performance.

In recent years, heteroatom doping has been widely used in electrochemical energy storage devices, which can greatly improve the surface properties of electrode materials, shorten the ion transport channels, and thus significantly improve the charge storage capability,<sup>23,24</sup> which include (N or S)-doped graphene,<sup>25</sup> (B, N or S)-doped hard carbon,<sup>26</sup> and S-doped  $V_6O_{13-x}$  (VOS).<sup>27</sup> Furthermore, vacancy defects can increase the number of electroactive sites and enhance the electron/ion transfer kinetics of electrode materials,<sup>23,24</sup> such as O-vacancy- $Co_3O_4$ ,<sup>28</sup> and Co-vacancy- $CoSe_2$ .<sup>29</sup> Considering the above advantages, the Li/Na-ion storage capability of the pristine  $MnF_2$  anode can be significantly increased by simultaneously introducing hetero oxygen-doping and intrinsic fluorine anion-vacancies.

In this work, we report hetero oxygen-doping and fluorine anion-vacancy double-defective Mn–O–F ultrafine nanowires as novel promising anodes for LICs and NICs. Due to the disadvantages of large particle size and low specific surface area of pristine  $MnF_2$ , we propose a simple method to solve these problems *via* the etching treatment of pristine  $MnF_2$  micro/nanocrystals with  $NaBH_4$  agents, which generates double-defective Mn–O–F ultrafine nanowires with high porosity and large specific surface area (the materials are denoted as  $MnF_2$ -E). The performance of  $MnF_2$  candidates was firstly optimized *via* an orthogonal experiment ( $L_93^4$ ). The optimal  $MnF_2$  (8#) and etched  $MnF_2$  (8#)-E (Mn–O–F) anodes and commercial activated carbon (AC) cathode were used to construct the  $MnF_2$ //AC and  $MnF_2$ -E//AC LICs/NICs, which were optimized by tuning the active mass ratios of positive and negative electrodes and working voltage windows of the capacitors. Both the LICs and NICs based on the double-defective Mn–O–F anode showed much better electrochemical performance than the devices based on the  $MnF_2$  anode. The kinetics and mechanisms of the  $MnF_2$  and Mn–O–F anodes for both Li-ion and Na-ion storage were also investigated. Overall, this work addresses new insight into heteroatom doping and anion vacancy double-defective Mn–O–F anodes for advanced LICs and NICs and will have a significant impact on the development of advanced electrode materials for high-performance electrochemical energy storage devices.

## Results and discussion

### Physicochemical property

The optimal  $MnF_2$  8# (herein, the choice of  $MnF_2$  8# is owing to its overall superior specific capacity, rate capability and cycling behavior, Fig. S6 and Table S4, ESI†) and  $MnF_2$  8#-E (Mn–O–F)

materials were characterized by X-ray diffraction (XRD), Fourier transform infrared spectroscopy (FTIR), X-ray photoelectron spectroscopy (XPS), scanning electron microscopy (SEM), transmission electron microscopy (TEM), high-resolution TEM (HRTEM), selected area electron diffraction (SAED), X-ray energy dispersive spectroscopy (EDS), mapping, and nitrogen isothermal sorption with Brunauer–Emmett–Teller (BET) and Barrett–Joyner–Halenda (BJH) methods. Fig. 1A shows the XRD patterns of the  $MnF_2$  8# and  $MnF_2$  8#-E samples, which correspond to tetragonal  $MnF_2$  with the space group of  $P4_2/mnm$  (the crystal structures of  $MnF_2$  8# and  $MnF_2$  8#-E are shown in Fig. S1†). The XRD patterns of the other eight samples from the orthogonal experiment (Fig. S2 and Tables S1, S2†) also correspond to the tetragonal  $MnF_2$  standard card, indicating the successful synthesis of the materials. It is apparent that the peak intensity of  $MnF_2$  8#-E is significantly weaker than that of  $MnF_2$  8#, which indicates that the particle size or crystallinity of the  $MnF_2$  8#-E sample decreased significantly. More interestingly, in the enlarged view of the crystal plane of (110), the peak position of  $MnF_2$  8#-E shows a slight negative shift by  $0.03^\circ$ , which may be due to oxygen heteroatom doping. The IR spectra of  $MnF_2$  8#-E and  $MnF_2$  8# in Fig. 1B demonstrate the presence of the Mn–O bond in  $MnF_2$  8#-E, which is direct evidence of the oxygen heteroatom doping. Fig. 1C shows the XPS survey scan spectra of  $MnF_2$  8# and  $MnF_2$  8#-E. The typical Mn 2p and F 1s can be clearly seen for  $MnF_2$ . Notably, the O 1s peak of  $MnF_2$  8#-E is significantly stronger than that of  $MnF_2$  8#, whereas the F 1s peak of  $MnF_2$  8#-E is obviously weaker than that of  $MnF_2$  8#, which is attributed to the fact that the oxygen heteroatoms largely occupy the positions of the fluorine atoms, resulting in the presence of rich fluorine vacancies owing to the charge

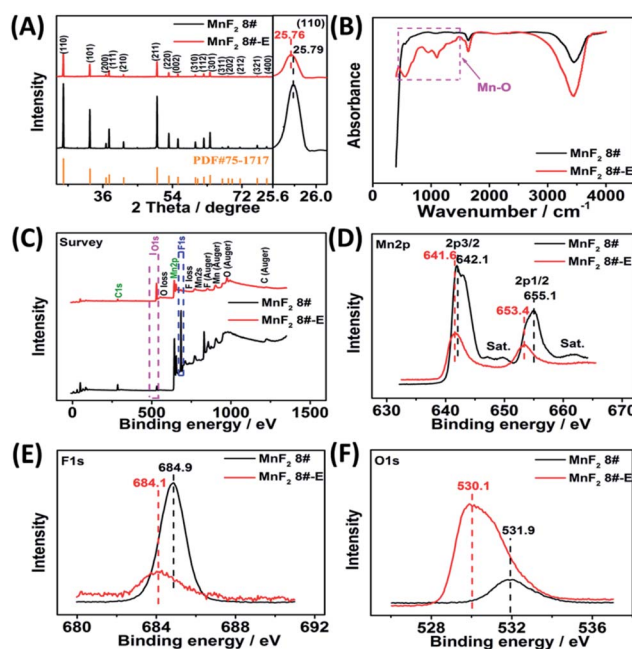


Fig. 1 XRD patterns(A), FTIR spectra (B), XPS survey scan (C), and XPS Mn 2p (D), F 1s (E) and O 1s (F) spectra of the  $MnF_2$  8# and  $MnF_2$  8#-E samples.



balance. The Mn 2p spectra of MnF<sub>2</sub> 8# and MnF<sub>2</sub> 8#-E are shown in Fig. 1D, where Mn 2p<sub>3/2</sub> and Mn 2p<sub>1/2</sub> are negatively shifted by 0.6 eV and 1.7 eV compared with the Mn 2p spectra of MnF<sub>2</sub> 8#, respectively, which is due to the formation of the Mn–O bond by oxygen doping. The F 1s spectrum of MnF<sub>2</sub> 8#-E in Fig. 1E is significantly lower than that of MnF<sub>2</sub> 8#, accompanied by a negative shift of 0.8 eV for MnF<sub>2</sub> 8#-E, which is due to the hetero oxygen doping and fluorine ion vacancy. Fig. 1F shows the O 1s spectra, where the O 1s peak of MnF<sub>2</sub> 8#-E exhibits a negative shift of 1.8 eV compared to that of MnF<sub>2</sub> 8#, which is due to the formation of a strong Mn–O bond by the hetero oxygen doping. Moreover, the ratio of Mn/O/F was estimated to be 1:0.934/0.132 based on the XPS results, and thus the formula of Mn–O–F can be expressed as MnO<sub>0.934</sub>F<sub>0.132</sub>. Herein, the doping of oxygen heteroatoms and fluorine vacancy double defects gave Mn–O–F a distinct advantage in electrochemical performance.

The SEM and TEM images of MnF<sub>2</sub> 8# are shown in Fig. 2A and B, respectively, showing a size range of around 0.5–2 μm. The HRTEM image of MnF<sub>2</sub> 8# in Fig. 2C shows the lattice fringes of 0.345 nm, which is matched with the (110) crystal plane of tetragonal MnF<sub>2</sub>. The SAED patterns in Fig. 2D exhibit the single-crystalline diffraction characteristics of MnF<sub>2</sub> 8# with the marked standard crystalline planes of (110), which are in

good agreement with the HRTEM and XRD results. Furthermore, the mapping images of MnF<sub>2</sub> 8# in Fig. 2E–G demonstrate the uniform distributions of F/Mn species. Fig. 2H, I and S3† show the SEM/TEM images of MnF<sub>2</sub> 8#-E, which exhibit an ultrafine nanowire morphology with a diameter of about 10 nm, and a much more porous structure can be clearly seen for MnF<sub>2</sub> 8#-E (the possible formation process can be seen in Scheme 1, ESI†), which endows the MnF<sub>2</sub> 8#-E sample with more electroactive sites than the pristine MnF<sub>2</sub> 8# sample. The ultrafine nanowire morphology and porous structure also ensure a shorter ion transport length and provide a larger electrode/electrolyte interface for charge transport reactions, which is also reflected in its superior electrochemical performance.<sup>30</sup> The HRTEM image and SAED pattern of MnF 8#-E are shown in Fig. 2J and K, respectively, in which a typical amorphous

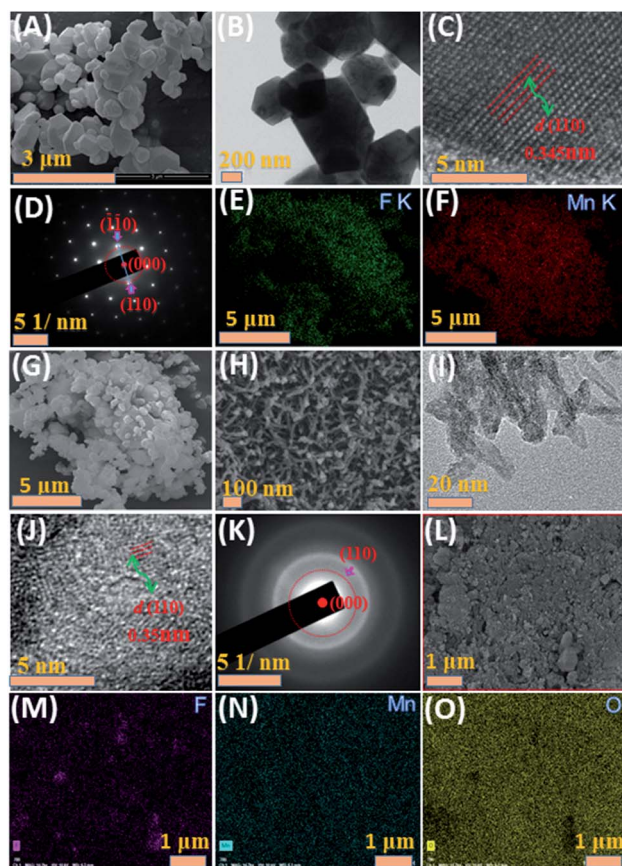
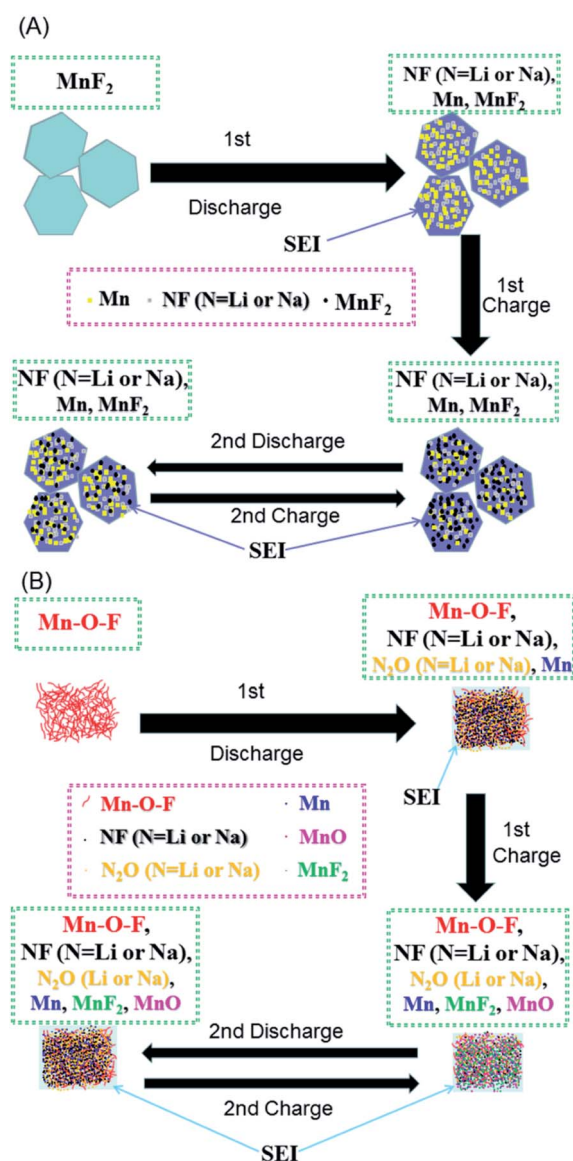


Fig. 2 SEM (A), TEM (B), HRTEM (C), SAED (D) and mapping (E–G) images of MnF<sub>2</sub> 8# sample. SEM (H), TEM (I), HRTEM (J), SAED (K) and mapping (L–O) images of MnF<sub>2</sub> 8#-E sample.



Scheme 1 Schematics of the possible reaction mechanisms for the MnF<sub>2</sub> (A) and MnF<sub>2</sub>-E (B) electrodes during the first two cycles of discharging/charging processes.





structure with a lightly larger lattice fringe of 0.35 nm corresponding to the (110) crystal plane can be detected. The mapping diagrams of  $\text{MnF}_2$  8#-E in Fig. 2L–O demonstrate the even distribution of Mn, O, and F elements in the  $\text{MnF}_2$  8#-E sample, which again prove hetero oxygen doping in the  $\text{MnF}_2$  structure. The different colors of  $\text{MnF}_2$  8# and  $\text{MnF}_2$  8#-E in Fig. S4† and the element results from the EDS data in Fig. S5† also reflect the doping of oxygen heteroatoms and the change in the intrinsic structure of the materials. Further changes can be also seen from the nitrogen isothermal sorption data, pore volume and pore size distribution of  $\text{MnF}_2$  8# and  $\text{MnF}_2$  8#-E (Fig. 3A–F). Specifically,  $\text{MnF}_2$  8# has a very small specific surface area of only  $2.75 \text{ m}^2 \text{ g}^{-1}$ , while  $\text{MnF}_2$  8#-E exhibits a staggering value of  $198.96 \text{ m}^2 \text{ g}^{-1}$ , and the pore volume of  $\text{MnF}_2$  8# is also very small ( $0.008 \text{ cm}^3 \text{ g}^{-1}$ ) in comparison with the very large pore volume of  $\text{MnF}_2$  8#-E ( $0.95 \text{ cm}^3 \text{ g}^{-1}$ ), and the pore size of  $\text{MnF}_2$  8# is mainly distributed at 2.23 nm in comparison with the bigger pore size distribution of  $\text{MnF}_2$  8#-E (11.26 nm), which indicate an enormous increase in specific surface area, pore volume and pore size by the introduction of hetero oxygen doping and fluorine vacancy double defects, ensuring the exceptionally superior electrochemical performance of the double-defective Mn–O–F ultrafine nanowires for Li/Na-ion storage.

### Performance for Li-ion storage

To evaluate the electrochemical performance of the  $\text{MnF}_2$  (1#–9#) samples and select the optimal candidate from the orthogonal experiments, Li// $\text{MnF}_2$  half cells were assembled and

tested *via* cyclic voltammetry (CV) and galvanostatic charge/discharge (GCD) between 0.01 and 3 V (vs.  $\text{Li/Li}^+$ ). Based on the results of the orthogonal analysis and performance comparison in Tables S3, S4 and Fig. S6,†  $\text{MnF}_2$  8# exhibited an overall superior performance. The cyclic voltammogram of the first three revolutions at  $0.1 \text{ mV s}^{-1}$  of  $\text{MnF}_2$  8# is shown in Fig. 4A, with one minor peak located at about 0.96 V and a sharp peak at around 0.29 V for the first cathode scan, which coincide with the platforms and the sloped regions at the low voltage appearing in the original discharge branch of the GCD curves at  $0.1 \text{ A g}^{-1}$  (Fig. 4B), respectively. These peaks are largely owing to the conversion of  $\text{MnF}_2$  into  $\text{Mn/LiF}$  and the formation of solid electrolyte interphase (SEI) films accompanied with a highly reversible interfacial Li-ion intercalation reaction within the  $\text{Mn/LiF}$  matrix in the low potential region, respectively.<sup>31–35</sup> Also, the minor anodic peak at 1.01 V can be ascribed to the partial conversion of  $\text{Mn/LiF}$  into  $\text{MnF}_2$ .<sup>31,32</sup> However, the redox peaks

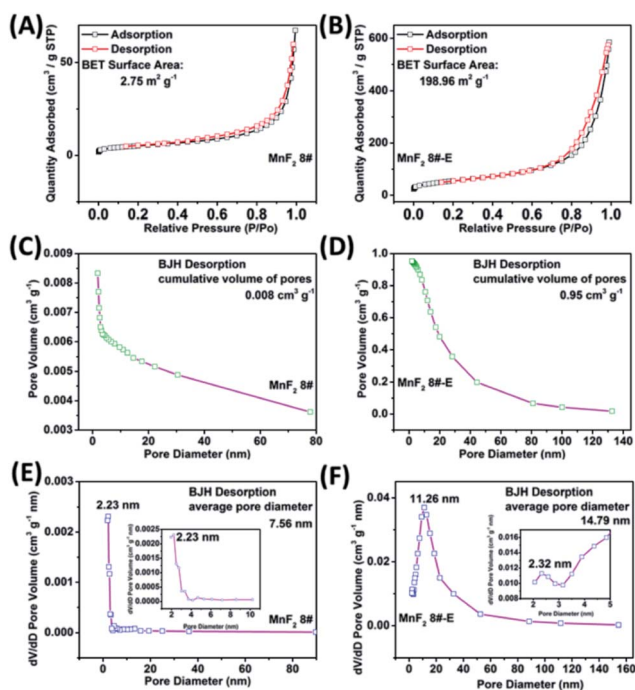


Fig. 3  $\text{N}_2$  isothermal sorption (A and B), pore volume (C and D) and pore size distribution (E and F) of the  $\text{MnF}_2$  8# and  $\text{MnF}_2$  8#-E samples, respectively.

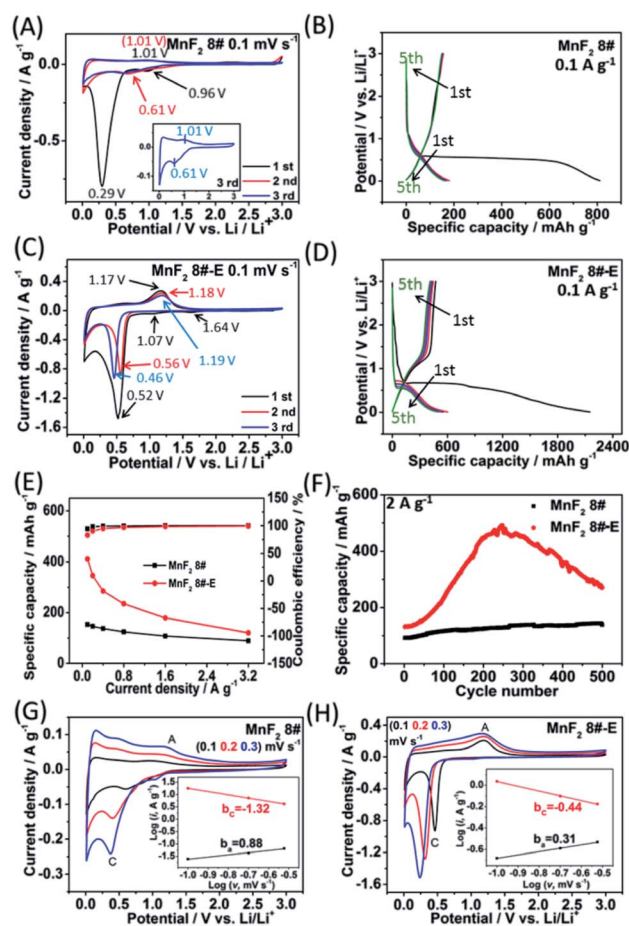


Fig. 4 CV plots for the first three cycles at  $0.1 \text{ mV s}^{-1}$  (A) and GCD curves for the 5th cycle at  $0.1 \text{ A g}^{-1}$  (B) of  $\text{MnF}_2$  8# electrode, CV plots for the first three cycles at  $0.1 \text{ mV s}^{-1}$  (C) and GCD curves for the 5th cycle at  $0.1 \text{ A g}^{-1}$  (D) of  $\text{MnF}_2$  8#-E electrode, specific capacity and coulombic efficiency derived from the respective 5th cycle at  $0.1$ – $3.2 \text{ A g}^{-1}$  of  $\text{MnF}_2$  8# and  $\text{MnF}_2$  8#-E electrodes (E), cycling stability for 500 cycles at  $2 \text{ A g}^{-1}$  of  $\text{MnF}_2$  8# and  $\text{MnF}_2$  8#-E electrodes (F), and CV plots for the 3rd cycle at 0.1, 0.2, and  $0.3 \text{ mV s}^{-1}$  of  $\text{MnF}_2$  8# and  $\text{MnF}_2$  8#-E (insets show the plots of  $\lg i$  vs.  $\lg v$ ) (G and H).

were maintained at about 1.01/0.61 V in the subsequent cycles, and it can be seen from the charge–discharge curves that the capacity is basically unchanged in the subsequent cycles except for the much larger specific capacity of the original discharge, indicating that the internal structure is protected after the formation of the SEI films, and shows good electrochemical stability.<sup>31,32</sup> Similar changing trends in the redox peaks and charge–discharge platforms can be also found from the CV curves and GCD plots of the other MnF<sub>2</sub> samples, as shown in Fig. S7 and S8.†

Fig. 4C shows the CV plots of MnF<sub>2</sub> 8#-E at a sweep speed of 0.1 mV s<sup>-1</sup>, with two weak cathode peaks at 1.64 V and 1.07 V and a sharp cathode peak at 0.52 V in the first cathode sweep, which may be due to the conversion of Mn–O–F into Mn/LiF/Li<sub>2</sub>O and the formation of the SEI films, and the minor anodic peak at 1.17 V can be ascribed to the partial conversion of Mn/LiF/Li<sub>2</sub>O into MnF<sub>2</sub>/MnO.<sup>14,31,32</sup> In the next two cycles, the cathode peaks shifted slightly from 0.56 V to 0.46 V, and the anode peaks shifted slightly from 1.18 V to 1.19 V, indicating good reversibility. Fig. 4E and F show the specific capacity and cycle performance of the MnF<sub>2</sub> 8# and MnF<sub>2</sub> 8#-E electrodes, respectively, where MnF<sub>2</sub> 8#-E provided the much bigger specific capacity of 411–120 mA h g<sup>-1</sup> at 0.1–3.2 A g<sup>-1</sup> in comparison with that of 153–89 mA h g<sup>-1</sup> at 0.1–3.2 A g<sup>-1</sup> for the MnF<sub>2</sub> 8# electrode. The more obvious gap is also reflected in the cycle performance after 500 cycles at 2 A g<sup>-1</sup>, where MnF<sub>2</sub> 8#-E exhibited 271 mA h g<sup>-1</sup> (207% retention), whereas MnF<sub>2</sub> 8# exhibited only 138 mA h g<sup>-1</sup> (152% retention). Moreover, the performance of the Mn–O–F anode is comparable or even superior to that of many state-of-the-art anode materials for Li-ion batteries (LIBs) (Table S5, ESI†) (the more detailed performance from the CV curves, GCD curves, rate capability and coulombic efficiency, cycling stability and coulombic efficiency of the MnF<sub>2</sub> (1#–9#) and MnF<sub>2</sub> 8#-E electrodes can be seen in Fig. S7–S14†). The enhanced performance of the Mn–O–F ultrafine nanowires with the hetero oxygen doping and fluorine vacancies provides an important strategy for the promotion of charge storage capability of Li-ion anode materials. Herein, the initial increase in capacity for the MnF<sub>2</sub> 8# and MnF<sub>2</sub> 8#-E electrodes may be owing to the formation of continuous conductivity networks *via* the conversion, reversible reactions of SEI films and enhanced electroactive sites by the activation of the electrode,<sup>32</sup> while the subsequent decrease in capacity for the MnF<sub>2</sub> 8#-E electrode may be owing to the decrease in the electroactive sites by the agglomeration of the amorphous ultrafine nanoparticles. The XRD patterns of the electrodes after cycling (Fig. S15A and B, ESI†) demonstrate the very faint diffraction peaks of MnF<sub>2</sub> phase compared with the pristine states, and the TEM images of the electrodes after cycling (Fig. S15C–F, ESI†) show the presence of numerous ultrafine nanoparticles in the pristine nanocrystals or nanowires, suggesting the formation of a largely amorphous nanostructure for Li-ion storage after the long-term conversions. The CV plots at different sweep rates (0.1, 0.2, and 0.3 mV s<sup>-1</sup>) of the MnF<sub>2</sub> 8# and MnF<sub>2</sub> 8#-E electrodes are shown in Fig. 4G and H, and the relationship of lg *i*–lg *v* (*i* = *av*<sup>*b*</sup>)<sup>36</sup> for MnF<sub>2</sub> 8# and MnF<sub>2</sub> 8#-E electrodes derived from the CV plots are shown in the insets of

Fig. 4G and H. Note that the slopes of *ba* and *bc* are 0.88 and –1.32 for MnF<sub>2</sub> 8#, in comparison with that of 0.31 and –0.44 for MnF<sub>2</sub> 8#-E, respectively. These results indicate that the kinetics of the MnF<sub>2</sub> 8# electrode is dominated by surface-controlled kinetics (*i.e.* pseudocapacitive behavior),<sup>37</sup> whereas the MnF<sub>2</sub> 8#-E electrode has the typical diffusion-controlled property. Herein, the absolute *b* values (0.31/0.44) of the MnF<sub>2</sub> 8#-E electrode are lower than 0.5, indicating the deviation from the typical planar diffusion characteristics, which may be owing to the highly porous and rough structure of the electrode, leading to the partial spherical diffusion. Moreover, the pseudocapacitive contribution (*k<sub>1</sub>v*)<sup>36,37</sup> at 0.1–0.3 mV s<sup>-1</sup> was estimated to be 73–82% and 31–44% for the MnF<sub>2</sub> 8# and MnF<sub>2</sub> 8#-E electrodes, respectively (Fig. S16 and S17, ESI†).

Electrochemical impedance spectroscopy (EIS) was used to investigate the electrochemical kinetics of the MnF<sub>2</sub> and MnF<sub>2</sub> 8#-E electrodes for Li-ion storage. As shown in Fig. S19,† the Nyquist plots include a Z'-axis intercept at the superhigh frequency, one semicircle in the high frequency region, a short sloping line in the intermediate frequency region and an oversized curved arc in the low frequency region, which are considered as the internal ohmic resistance (*R<sub>s</sub>*) (including resistances of electrode and electrolyte, and contact resistances between particles and/or between electrode and current collector), charge transfer resistance (*R<sub>ct</sub>*) related to the electrochemical kinetics process, Warburg impedance (*W*) related to the ion diffusion process and the electronic resistance related to the bulk materials, respectively.<sup>32</sup> The equivalent circuit model is shown in Fig. S18 (ESI†), and the fitting results are listed in Table S6 (ESI†), in which the Mn–O–F electrode shows a smaller *R<sub>ct</sub>* (37.33 Ω) than the MnF<sub>2</sub> electrodes (43.09–68.34 Ω), implying the faster electrochemical kinetics in the Mn–O–F electrode because of its superior morphology and porosity.

The MnF<sub>2</sub>/AC and MnF<sub>2</sub>-E//AC LICs were further assembled with MnF<sub>2</sub> 8# and MnF<sub>2</sub> 8#-E as the anodes and commercial AC as the cathode together with the anodes pre-charged (pre-lithiation) mode at 0.1 A g<sup>-1</sup> for 3.5 turns (Fig. S20†). Different active mass ratios of the cathode/anode were examined firstly. For the MnF<sub>2</sub>/AC LICs, the performance comparison for different mass ratios in Fig. S22† makes it clear that MnF<sub>2</sub>/AC (1 : 1) is the optimal LIC (the performance of the AC cathode is shown in Fig. S21,† and the voltage windows, GCD curves and CV plots of the MnF<sub>2</sub>/AC LICs with different mass ratios are shown in Fig. S23 and S24†). For the MnF<sub>2</sub>-E//AC LICs, the best mass ratio was determined to be 1 : 2 based on the results shown in Fig. S25 and S26.† After selecting the optimal mass ratios of the LICs, different voltage windows (0–4 V and 0–4.3 V) were further examined. Fig. 5A–H show the CV plots at 40 mV s<sup>-1</sup>, GCD curves at 1 A g<sup>-1</sup>, Ragone behavior and cycling performance at 5 A g<sup>-1</sup> of the MnF<sub>2</sub>/AC (1 : 1) and MnF<sub>2</sub>-E//AC (1 : 2) LICs under the voltages of 0–4 V and 0–4.3 V. The MnF<sub>2</sub>-8#-E//AC capacitor exhibited a larger CV area and longer charge and discharge times, indicating its better performance (the CV plots at different sweep speeds and GCD curves under different current densities are shown in Fig. S26–S28†). Furthermore, the MnF<sub>2</sub>-E//AC LICs exhibited remarkable performances under both 0–4 V (106.8–41.4 W h kg<sup>-1</sup>/0.33–10.7 kW kg<sup>-1</sup>, 63.4%



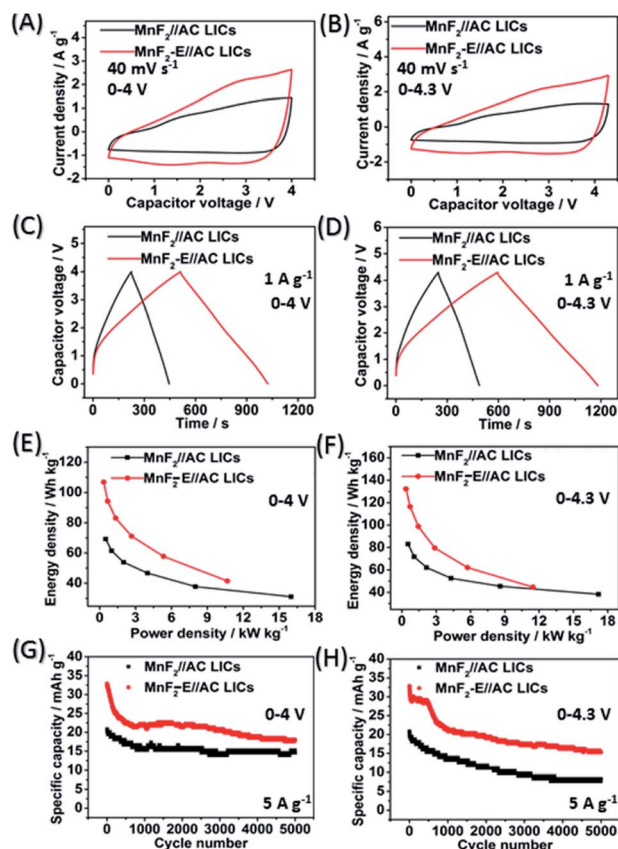


Fig. 5 CV plots at  $40 \text{ mV s}^{-1}$  (A and B), GCD curves at  $1 \text{ A g}^{-1}$  (C and D), Ragone plots (E and F) and cycling behavior for 5000 cycles at  $5 \text{ A g}^{-1}$  (G and H) of the  $\text{MnF}_2$  8#//AC and  $\text{MnF}_2$  8#-E//AC LICs under the voltages of 0–4 V and 0–4.3 V, respectively.

retention/3000 cycles/ $5 \text{ A g}^{-1}$ ) and 0–4.3 V ( $132.2\text{--}44.6 \text{ W h kg}^{-1}$ /  $0.36\text{--}11.5 \text{ kW kg}^{-1}$ , 63.5% retention/1000 cycles/ $5 \text{ A g}^{-1}$ ) in comparison with the  $\text{MnF}_2$ //AC LICs at 0–4 V ( $69.2\text{--}31.1 \text{ W h kg}^{-1}$ /  $0.5\text{--}16.0 \text{ kW kg}^{-1}$ , 72.5% retention/3000 cycles/ $5 \text{ A g}^{-1}$ ) and 0–4.3 V ( $82.9\text{--}38.2 \text{ W h kg}^{-1}$ /  $0.54\text{--}17.2 \text{ kW kg}^{-1}$ , 63.5% retention/1000 cycles/ $5 \text{ A g}^{-1}$ ) (more details are shown in Table S7†). The remarkable performance of the  $\text{MnF}_2$ -E//AC LICs further proves that the double-defective Mn–O–F ultra-fine nanowire anode with hetero oxygen doping and intrinsic fluorine vacancy greatly enhances the energy storage performance. Moreover, the  $\text{MnF}_2$ -E//AC and  $\text{MnF}_2$ //AC LICs exhibited comparable or even better performance than many state-of-the-art LICs systems reported in the literature (Table S8†), demonstrating their promising application in Li-ion storage.

### Performance for Na-ion storage

Due to the remarkable Li-ion storage capability of  $\text{MnF}_2$  8# and  $\text{MnF}_2$  8#-E, they were further investigated for Na-ion storage. In the CV plots of the  $\text{MnF}_2$  8# electrode at  $0.1 \text{ mV s}^{-1}$  (Fig. 6A), there was a big reduction peak at around 1.03 V and a small reduction peak at about 0.16 V, corresponding to the conversion of  $\text{MnF}_2$  into  $\text{Mn/NaF}$  and formation of SEI films in the first discharge, respectively. Moreover, the Na-ion storage capacity in

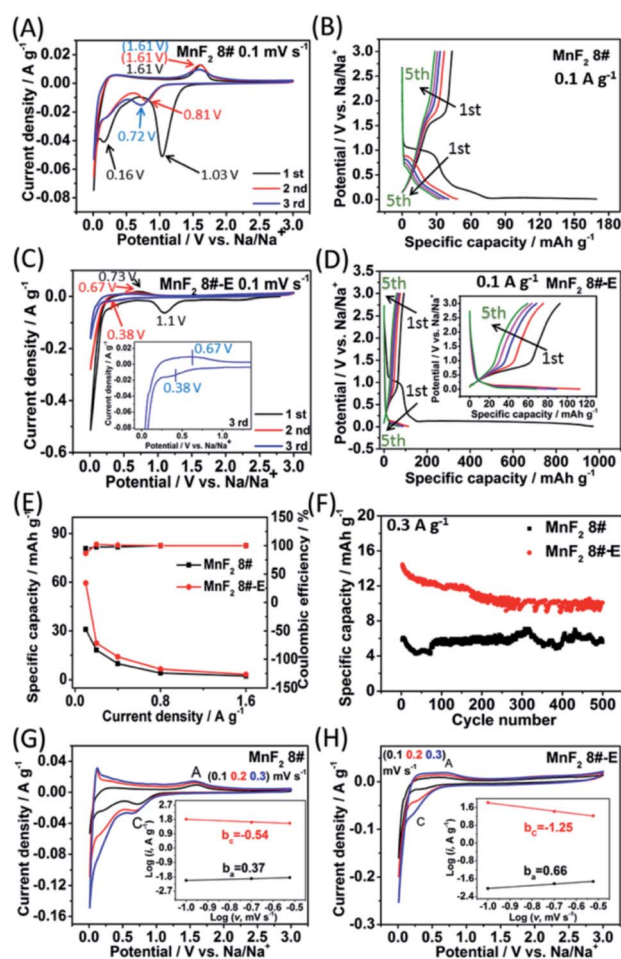


Fig. 6 CV plots for the first three cycles at  $0.1 \text{ mV s}^{-1}$  (A) and GCD curves for the 5th cycle at  $0.1 \text{ A g}^{-1}$  (B) of  $\text{MnF}_2$  8# electrode, CV plots for the first three cycles at  $0.1 \text{ mV s}^{-1}$  (C) and GCD curves for the 5th cycle at  $0.1 \text{ A g}^{-1}$  (D) of the  $\text{MnF}_2$  8#-E electrode, specific capacity and coulombic efficiency derived from the respective 5th cycle at 0.1– $1.6 \text{ A g}^{-1}$  of the  $\text{MnF}_2$  8# and  $\text{MnF}_2$  8#-E electrodes (E), cycling stability for 500 cycles at  $0.3 \text{ A g}^{-1}$  of the  $\text{MnF}_2$  8# and  $\text{MnF}_2$  8#-E electrodes (F), and CV plots for the 3rd cycle at 0.1, 0.2, and  $0.3 \text{ mV s}^{-1}$  of  $\text{MnF}_2$  8# and  $\text{MnF}_2$  8#-E (insets show the plots of  $\lg i$  vs.  $\lg v$ ) (G and H).

the low potential region also originated from a reversible interfacial Na-ion intercalation reaction within the  $\text{Mn/NaF}$  matrix as Li-ion intercalation.<sup>31–35</sup> Also, the minor anodic peak at about 1.61 V can be ascribed to the partial conversion of  $\text{Mn/NaF}$  into  $\text{MnF}_2$ . In the second and third laps, the reduction peaks changed lightly from 0.81 V to 0.72 V, and the oxidation peaks were basically maintained at 1.61 V, indicating good reversibility. Fig. 6C shows the CV plots of the  $\text{MnF}_2$  8#-E electrode at a sweep speed of  $0.1 \text{ mV s}^{-1}$ . A large cathode peak can be observed at about 1.1 V and small peak at around 0.4 V in the first round of negative sweep, which can be attributed to the conversion of  $\text{Mn–O–F}$  into  $\text{Mn/NaF/Na}_2\text{O}$  and the formation of SEI films, respectively. Also, the minor anodic peak at 0.73 V during the first positive sweep can be ascribed to the partial conversion of  $\text{Mn/NaF/Na}_2\text{O}$  into  $\text{MnF}_2/\text{MnO}$ . During the next two turns, the cathode peaks were basically maintained at





0.38 V, while the anode peaks shifted lightly from 0.73 V to 0.67 V, indicating good reversibility. Fig. 6B and D show the GCD curves for the  $\text{MnF}_2$  8# and  $\text{MnF}_2$  8#-E electrodes in the first five laps of  $0.1 \text{ A g}^{-1}$ , where the charge/discharge characteristics with the potential platforms coincide with the anodic/cathodic processes with redox peaks in their CV plots. Notably, the potential platforms of the  $\text{MnF}_2$  8#-E electrode are obviously lower than that of the  $\text{MnF}_2$  8# electrode for Na-ion storage, implying the superiority of the charge storage of the Mn-O-F anode. Fig. 6E and F show the gradient specific capacity and cycle behavior for the  $\text{MnF}_2$  8# and  $\text{MnF}_2$  8#-E electrodes, where  $\text{MnF}_2$  8# provides  $31\text{--}2 \text{ mA h g}^{-1}$  at  $0.1\text{--}3.2 \text{ A g}^{-1}$  with  $5.4 \text{ mA h g}^{-1}$  after 500 cycles at  $0.3 \text{ A g}^{-1}$  in comparison with the performance of  $59\text{--}4 \text{ mA h g}^{-1}$  at  $0.1\text{--}3.2 \text{ A g}^{-1}$  with  $11 \text{ mA h g}^{-1}$  after 500 cycles at  $0.3 \text{ A g}^{-1}$  for  $\text{MnF}_2$  8#-E (more details are shown in Fig. S29 and S30; Table S4<sup>†</sup>), which again shows that the double-defective Mn-O-F ultrafine nanowires anodes exhibit a big advantage in Na-ion storage. The XRD patterns of the electrodes after cycling (Fig. S31A and B<sup>†</sup>) show the slightly smaller diffraction peaks of the  $\text{MnF}_2$  phase, and the TEM images of the electrodes after cycling (Fig. S31C-F<sup>†</sup>) show the presence of a few of ultrafine nanoparticles in the pristine nanocrystals or nanowires, suggesting the formation of partially amorphous nanostructural products for Na-ion storage after the long-term conversions. Fig. 6G and H show the CV plots at different sweep speeds and the relationship between peak current density and sweep rate ( $\lg i = b \lg v + a$ ) for the  $\text{MnF}_2$  8# and  $\text{MnF}_2$  8#-E electrodes, respectively. The  $ba$  and  $bc$  values for the  $\text{MnF}_2$  8# electrode are 0.37 and  $-0.54$ , respectively, suggesting the typical diffusion-controlled kinetics, and the  $ba$  and  $bc$  values for the  $\text{MnF}_2$  8#-E electrode are 0.66 and  $-1.25$ , respectively, implying the dominant surface-controlled kinetics. Herein, the kinetic behavior of the  $\text{MnF}_2$  8# and  $\text{MnF}_2$  8#-E electrodes showed obvious differences between Li-ion storage (surface control/diffusion control) and Na-ion storage (diffusion control/surface control), which may be due to the difference in the radius of the Na and Li ions and the surface morphology and structure of the  $\text{MnF}_2$  8# and  $\text{MnF}_2$  8#-E materials. Moreover, the pseudocapacitive contribution ( $k_1v$ )<sup>36,37</sup> at  $0.1\text{--}0.3 \text{ mV s}^{-1}$  was estimated to be 72–82% and 15–24% for the  $\text{MnF}_2$  8# and  $\text{MnF}_2$  8#-E electrodes (Fig. S32 and S33, ESI<sup>†</sup>), respectively. The electrochemical kinetics of the  $\text{MnF}_2$  8# and Mn-O-F electrodes for Na-ion storage were further analyzed *via* EIS tests (Fig. S34 and Table S9, ESI<sup>†</sup>), which show that the Mn-O-F electrode possessed a smaller  $R_{\text{ct}}$  ( $106.7 \Omega$ ) than the  $\text{MnF}_2$  electrode ( $144.8 \Omega$ ), suggesting the faster electrochemical kinetics of the Mn-O-F electrode owing to its superior morphology and porosity.

The  $\text{MnF}_2$ //AC and  $\text{MnF}_2$ -E//AC NICs were also assembled with  $\text{MnF}_2$  8# and  $\text{MnF}_2$  8#-E as anodes and commercial AC as the cathode along with the anodes pre-charged (pre-sodiation) at  $0.1 \text{ A g}^{-1}$  for 3.5 turns (Fig. S35<sup>†</sup>). Initially, different active mass ratios of the cathode/anode were examined. The performance comparison for the different mass ratios in Fig. S37<sup>†</sup> indicate that the  $\text{MnF}_2$ //AC (1 : 1) NICs exhibited overall superior behavior (the performance of the AC cathode is shown in Fig. S36,† and the voltage windows, GCD curves and

CV plots of the  $\text{MnF}_2$ //AC NICs with different mass ratios are shown in Fig. S38 and S39<sup>†</sup>). The different potential windows were further examined under the optimal mass ratios of the NICs. Fig. 7A–H show the CV plots at  $40 \text{ mV s}^{-1}$ , GCD curves at  $1 \text{ A g}^{-1}$ , Ragone plots, and cycling behavior at  $3 \text{ A g}^{-1}$  for 800 cycles of the NICs under the voltages of 0–4 V and 0–4.3 V. The  $\text{MnF}_2$  8#-E//AC capacitor exhibited a larger CV area and longer charge and discharge times, indicating its better performance (the CV plots at different sweep speeds and GCD curves under different current densities are shown in Fig. S40 and S41,† respectively). The  $\text{MnF}_2$  8#-E//AC NICs exhibited a remarkable performance of  $42.1\text{--}8.9 \text{ W h kg}^{-1}/0.5\text{--}8.0 \text{ kW kg}^{-1}$ , and 63.1% retention/200 cycles/ $3 \text{ A g}^{-1}$  under 0–4 V and  $55.9\text{--}19.2 \text{ W h kg}^{-1}/0.48\text{--}7.7 \text{ kW kg}^{-1}$ , and 45.3% retention/200 cycles/ $3 \text{ A g}^{-1}$  under 0–4.3 V in comparison with that of the  $\text{MnF}_2$  8#//AC NICs ( $16.4\text{--}4.4 \text{ W h kg}^{-1}/0.5\text{--}8.0 \text{ kW kg}^{-1}$ , 50.2% retention/200 cycles/ $3 \text{ A g}^{-1}/0\text{--}4 \text{ V}$  and  $37\text{--}7.2 \text{ W h kg}^{-1}/0.54\text{--}8.6 \text{ kW kg}^{-1}$ , 66.7% retention/200 cycles/ $3 \text{ A g}^{-1}/0\text{--}4.3 \text{ V}$ , respectively). Furthermore, the  $\text{MnF}_2$ -E//AC NICs and  $\text{MnF}_2$ //AC NICs exhibited comparable or even better overall performances than that of many state-of-the-art NICs systems reported in the literature (Table S10<sup>†</sup>), showing their promising application in Na-ion storage.

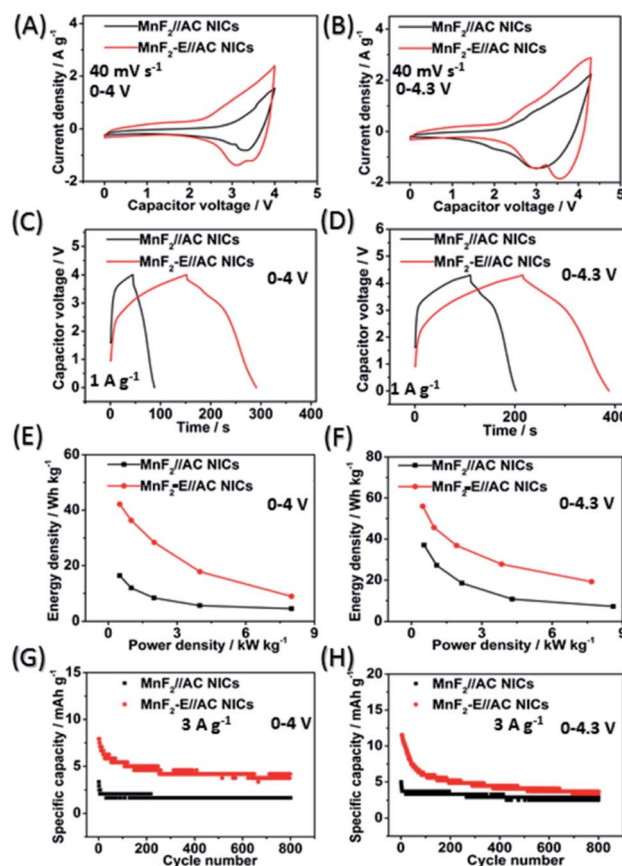


Fig. 7 CV plots at  $40 \text{ mV s}^{-1}$  (A and B), GCD curves at  $1 \text{ A g}^{-1}$  (C and D), Ragone plots (E and F), and cycling behavior for 800 cycles at  $3 \text{ A g}^{-1}$  (G and H) of  $\text{MnF}_2$  8#//AC and  $\text{MnF}_2$  8#-E//AC NICs under the voltages of 0–4 V and 0–4.3 V, respectively.



## Reaction mechanisms for Li/Na-ion storage

*Ex situ* X-ray photoelectron spectroscopy (XPS) was employed to investigate the possible reaction mechanisms of the  $\text{MnF}_2$  and  $\text{MnF}_2$ -E electrodes for both Li-ion and Na-ion storage. Fig. 8 shows the XPS data of the pristine, fully charged (3.0 V) and fully discharged (0.01 V) states of the  $\text{MnF}_2$  8# and  $\text{MnF}_2$  8#-E anodes

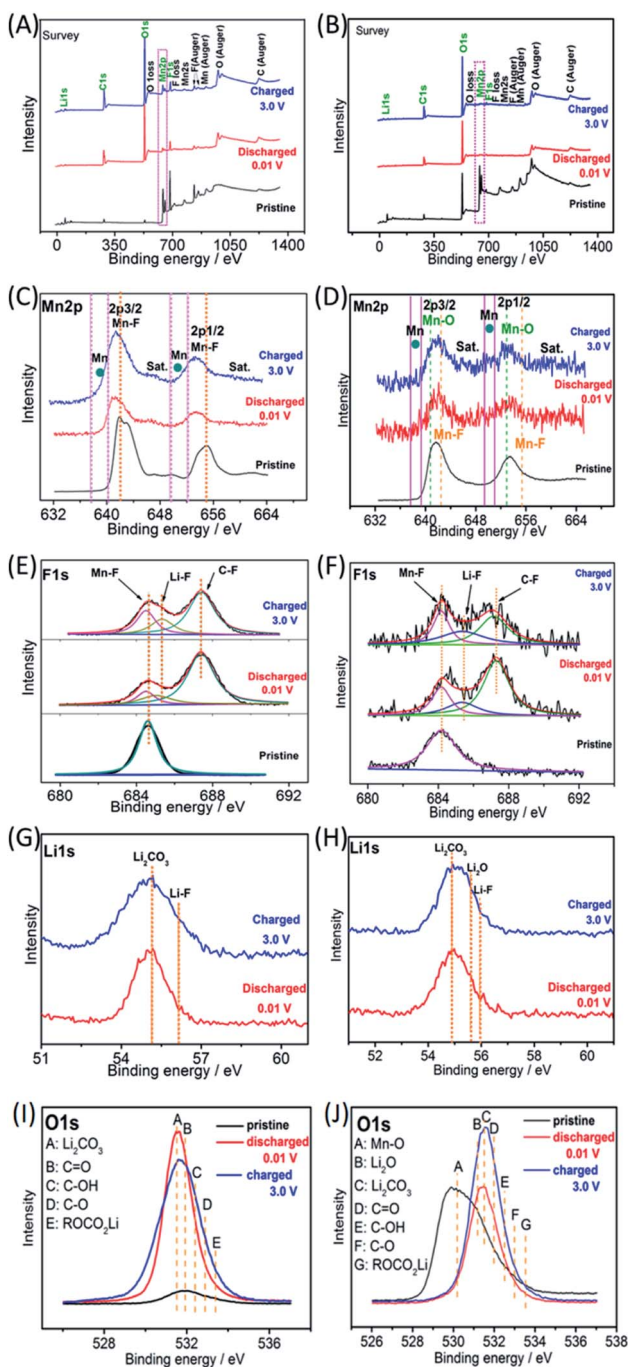


Fig. 8 *Ex situ* XPS spectra of  $\text{MnF}_2$  8# and  $\text{MnF}_2$  8#-E electrodes in the pristine, charged 3.0 and discharged 0.01 V states during the first discharging/charging cycle at  $0.05 \text{ A g}^{-1}$  for Li-ion storage: survey (A and B), Mn 2p (C and D), F 1s (E and F), Li 1s (G and H) and O 1s (I and J), respectively.

for the Li-ion storage. The survey scans in Fig. 8A and B, demonstrate the typical F 1s/Mn 2p/O 1s/C 1s in all three states. The much stronger C 1s/O 1s signals of  $\text{MnF}_2$  8# in the fully charged/discharged states than the pristine states is largely owing to the formation of SEI films with rich C/O-containing groups.<sup>32,38,39</sup> For  $\text{MnF}_2$  8#-E, the much stronger C 1s signal in the fully charged/discharged states is also owing to the formation of SEI films, while the strong O 1s signals in the fully charged/discharged states originate from both the SEI films and the pristine Mn–O bond. The Mn 2p spectra of  $\text{MnF}_2$  8# and  $\text{MnF}_2$  8#-E in Fig. 8C and D present the Mn  $2p_{3/2}$  and Mn  $2p_{1/2}$  peaks and corresponding shakeup satellite peaks (Sat.). Notably, the peak positions of Mn 2p showed some negative shifts for the fully discharged and charged states in comparison with that of the pristine states, indicating the partial conversion  $\text{MnF}_2$  and Mn–O–F into Mn metal phases during the discharging/charging processes.<sup>14,31</sup> Moreover, both the Mn–O and Mn–F bonds could be resolved for  $\text{MnF}_2$  8#-E in comparison with the sole Mn–F bond for  $\text{MnF}_2$  8#. The F 1s spectra in Fig. 8E and F reveal the Mn–F, Li–F and C–F (from polyvinylidene fluoride (PVDF) binder) bonds for the fully discharged/charged states in comparison with the Mn–F bonds in the pristine states. The Li 1s signals in Fig. 8G of the fully discharged and charged states originate from LiF and  $\text{Li}_2\text{CO}_3$  (from SEI films) during the discharging/charging processes.<sup>32,38,39</sup> Notably, additional  $\text{Li}_2\text{O}$  signals (except LiF and  $\text{Li}_2\text{CO}_3$ ) are present in the Li 1s spectra of  $\text{MnF}_2$  8#-E in Fig. 8H, which originated from one of the reaction products of Mn–O–F and Li-ion. Fig. 8I shows the O 1s spectra of  $\text{MnF}_2$  8#, which show a weak peak in the original state due to the presence of adsorbed oxygen (mainly  $\text{H}_2\text{O}$ , which can be also detected from the large –OH absorption peak appearing at  $3220 \text{ cm}^{-1}$  in the IR spectra of Fig. 1B). The O 1s became sharp under the fully charged/discharged states, which is attributed to the formation of SEI films (mainly including  $\text{Li}_2\text{CO}_3$ , C=O, C–OH, C–O and  $\text{ROCO}_2\text{Li}$ ).<sup>32,39</sup> Fig. 8J show the O 1s spectra of  $\text{MnF}_2$  8#-E, which exhibit a sharp Mn–O bond in its original state, the signals of  $\text{Li}_2\text{CO}_3$ , C=O, C–OH, C–O and  $\text{ROCO}_2\text{Li}$  in the fully charged/discharged states, suggesting the formation of SEI films, and the additional  $\text{Li}_2\text{O}$  in the fully charged/discharged states, indicating the reaction between Mn–O–F and Li-ion.

The Na-ion storage mechanisms of  $\text{MnF}_2$  and  $\text{MnF}_2$ -E were further investigated by *ex situ* XPS measurements of the pristine, fully discharged/charged states in the first cycle. As shown in Fig. 9A and B, the survey scans display the presence of Mn, F, O, Na, C and O species, indicating the reactions between  $\text{MnF}_2$  or Mn–O–F electrodes and Na-ion and the formation of SEI films. The Mn 2p spectra of  $\text{MnF}_2$  8# in Fig. 9C show the negative shift in the fully charged/discharged states and the presence of Mn, indicating a typical conversion reaction between the  $\text{MnF}_2$  and Na-ion. The Mn 2p spectra of  $\text{MnF}_2$  8#-E in Fig. 9D demonstrate the presence of Mn, Mn–F and Mn–O bonds, revealing the typical characteristics of the conversion reaction between the Mn–O–F and Na-ion. Fig. 9E and F show the F 1s spectra of  $\text{MnF}_2$  8# and  $\text{MnF}_2$  8#-E, respectively, where the typical Na–F, Mn–F and C–F (from PVDF) can be resolved,





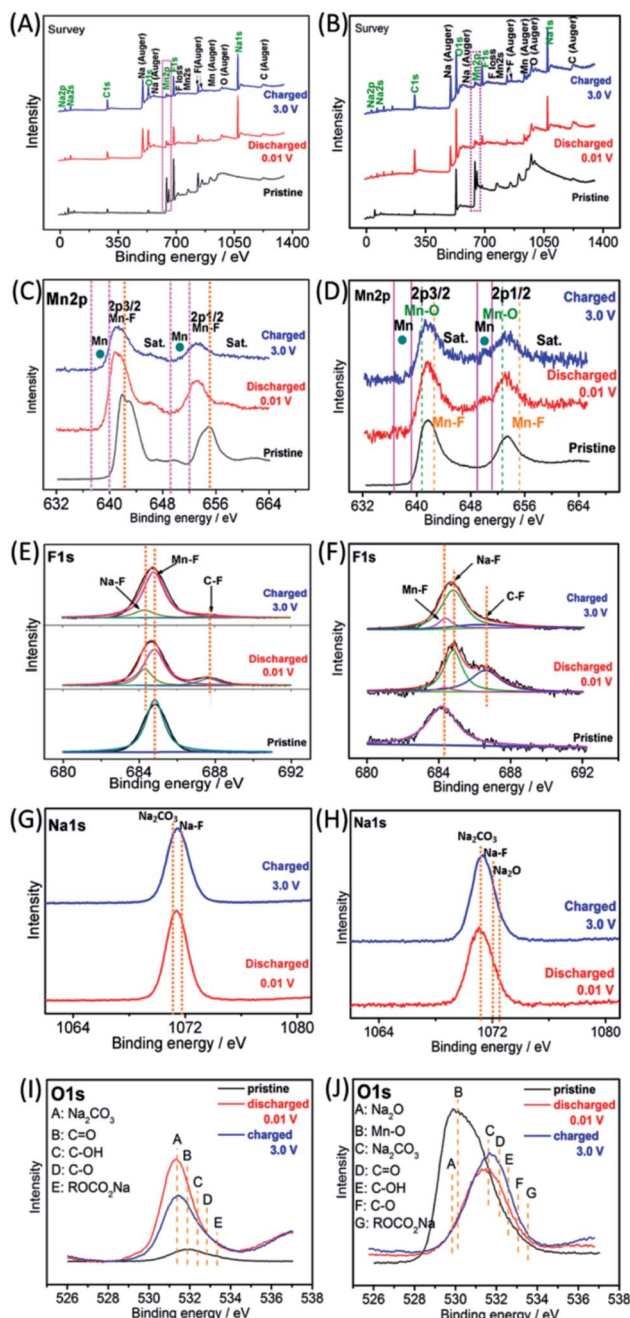
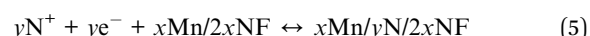
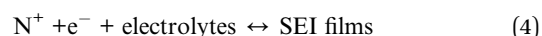
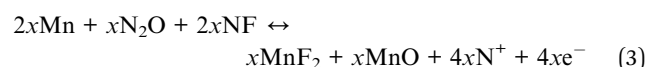
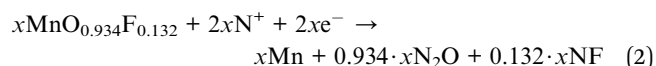
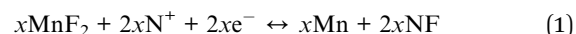


Fig. 9 *Ex situ* XPS spectra of MnF<sub>2</sub> 8# and MnF<sub>2</sub> 8#-E electrodes in the pristine, charged 3.0 V and discharged 0.01 V states during the first discharging/charging cycle at 0.02 A g<sup>-1</sup> for Na-ion storage: survey (A and B), Mn 2p (C and D), F 1s (E and F), Na 1s (G and H) and O 1s (I and J), respectively.

which again prove that MnF<sub>2</sub> 8# and MnF<sub>2</sub> 8#-E exhibit typical conversion reactions. The Na 1s spectra of MnF<sub>2</sub> 8# in Fig. 9G indicate the presence of NaF (mainly produced by the conversion reaction) and Na<sub>2</sub>CO<sub>3</sub> (from the SEI films). Fig. 9H shows the Na 1s spectra of MnF<sub>2</sub> 8#-E, where the Na<sub>2</sub>CO<sub>3</sub> bonds indicate the formation of SEI films, and NaF and Na<sub>2</sub>O were formed by the feature reactions of Mn–O–F with Na-ion. Fig. 9I shows the O 1s spectra of MnF<sub>2</sub>, where the Na<sub>2</sub>CO<sub>3</sub>, C=O, C–OH, C–O

and ROCO<sub>2</sub>Na bonds in both the fully discharged/charged states are due to the formation of SEI films.<sup>32,39</sup> Na<sub>2</sub>O is also detected in the O 1s spectra of fully discharged/charged MnF<sub>2</sub> 8#-E (Fig. 9J), which is derived from the feature reaction of Mn–O–F with Na-ion.

Based on the above considerations, the possible reaction mechanisms of the MnF<sub>2</sub> and Mn–O–F anodes for both Li-ion and Na-ion storage can be expressed as eqn (1)–(6). For MnF<sub>2</sub>, the mechanisms refer to eqn (1), (4) and (5) and for Mn–O–F, the mechanisms refer to eqn (2)–(6). A schematic of the possible processes for the first two discharging/charging cycles is illustrated in Scheme 1.



where N = Li, Na; 0 < x < 1; 0 < y < x.

## Conclusions

In summary, double-defective Mn–O–F ultrafine nanowires with hetero oxygen-doping and intrinsic fluorine-vacancies were introduced as advanced anodes for high-efficiency LICs and NICs. Owing to the unique doping-vacancy double defects, the Mn–O–F anode exhibited a superior performance than the pristine MnF<sub>2</sub> anode, contributing to the superior performance of the Mn–O–F//AC LICs/NICs than the corresponding MnF<sub>2</sub>//AC LICs/NICs. The *ex situ* characterizations and electrochemical methods revealed that the Mn–O–F anode demonstrates typical conversion reaction mechanisms with dominant diffusion-controlled and surface-controlled kinetics for Li/Na-ion storage, respectively. Overall, this work provides new insight into heteroatom-doping and anion vacancy double-defective Mn–O–F ultrafine nanowires anode to improve the Li/Na-ion storage and will have a significant impact on the development of advanced electrochemical energy storage devices.

## Conflicts of interest

There are no conflicts to declare.

## Acknowledgements

Thanks for the financial support from National Natural Science Foundation of China (21506182), Natural Science Foundation of Hunan Province (2018JJ2382), Education Department of Hunan



Province (18B077) and Hunan 2011 Collaborative Innovation Center of Chemical Engineering & Technology with Environmental Benignity and Effective Resource Utilization.

## Notes and references

- 1 J. M. Tarascon and M. Armand, *Nature*, 2001, **414**, 359–367.
- 2 Z. G. Yang, J. L. Zhang, M. W. KintnerMeyer, X. C. Lu, D. Choi, J. Lemmon and J. Liu, *Chem. Rev.*, 2011, **111**, 3577–3613.
- 3 J. Miller and P. Simon, *Science*, 2008, **321**, 651–652.
- 4 B. Li, J. S. Zheng, H. Y. Zhang, L. M. Jin, D. J. Yang, H. Lv, C. Shen, A. Shellikeri, Y. R. Zheng, R. Q. Gong, J. Zheng and C. M. Zhang, *Adv. Mater.*, 2018, **30**, 1705670.
- 5 H. W. Wang, C. R. Zhu, D. L. Chao, Q. Y. Yan and H. J. Fan, *Adv. Mater.*, 2017, **29**, 1702093.
- 6 J. Ding, W. B. Hu, E. Paek and D. Mitlin, *Chem. Rev.*, 2018, **118**, 6457–6498.
- 7 F. Li and Z. Zhou, *Small*, 2018, **14**, 1702961.
- 8 S. Natarajan, Y.-S. Lee and V. Aravindan, *Chem.-Asian J.*, 2019, **14**, 936–951.
- 9 P. Sennu, N. Arun, S. Madhavi, V. Aravindan and Y.-S. Lee, *J. Power Sources*, 2019, **414**, 96–102.
- 10 P. Pazhamalai, K. Krishnamoorthy, S. Sahoo and S.-J. Kim, *J. Alloys Compd.*, 2018, **765**, 1041–1048.
- 11 G. G. Amatucci, F. Badway, A. D. Pasquier and T. Zheng, *J. Electrochem. Soc.*, 2001, **148**, A930–A939.
- 12 S. Dsoke, B. Fuchs, E. Gucciardi and M. Wohlfahrt-Mehrens, *J. Power Sources*, 2015, **282**, 385–393.
- 13 P. Y. Wang, R. T. Wang, J. W. Lang, X. Zhang, Z. K. Chen and X. B. Yan, *J. Mater. Chem. A*, 2016, **4**, 9760–9766.
- 14 C. F. Liu, C. K. Zhang, H. Q. Song, C. P. Zhang, Y. G. Liu, X. H. Nan and G. Z. Cao, *Nano Energy*, 2016, **22**, 290–300.
- 15 D. P. Dubal, K. Jayaramulu, R. Zboril, R. A. Fischer and P. G. Romero, *J. Mater. Chem. A*, 2018, **6**, 6096–6106.
- 16 R. Ding, Q. Li and H. Y. Wang, *Electrochim. Acta*, 2013, **114**, 726–735.
- 17 N. Yabuuchi, K. Kubota, M. Dahbi and S. Komaba, *Chem. Rev.*, 2014, **114**, 11636–11682.
- 18 E. Lim, C. Jo, M. S. Kim, M. H. Kim, J. Y. Chun, H. Kim, J. Park, K. C. Roh, K. Kang, S. Yoon and J. Lee, *Adv. Funct. Mater.*, 2016, **26**, 3711.
- 19 H. X. Li, J. W. Lang, S. L. Lei, J. T. Chen, K. J. Wang, L. Y. Liu, T. Y. Zhang, W. S. Liu and X. B. Yan, *Adv. Funct. Mater.*, 2018, **28**, 1800757.
- 20 M. L. Kang, Y. Y. Wu, X. Huang, K. Q. Zhou, Z. G. Huang and Z. S. Hong, *J. Mater. Chem. A*, 2018, **6**, 22840–22850.
- 21 B. J. Yang, J. T. Chen, S. L. Lei, R. S. Guo, H. X. Li, S. Q. Shi and X. B. Yan, *Adv. Energy Mater.*, 2018, **8**, 1702409.
- 22 H. L. Wang, D. Mitlin, J. Ding, Z. Li and K. Cui, *J. Mater. Chem. A*, 2016, **4**, 5149–5158.
- 23 Y. L. Huang, Y. X. Zeng, M. H. Yu, P. Liu, Y. X. Tong, F. L. Cheng and X. H. Lu, *Small Methods*, 2018, **2**, 1700230.
- 24 D. F. Yan, Y. X. Li, J. Huo, R. Chen, L. M. Dai and S. Y. Wang, *Adv. Mater.*, 2017, **29**, 1606459.
- 25 S. B. Yang, L. J. Zhi, K. Tang, X. L. Feng, J. Maier and K. Müllen, *Adv. Funct. Mater.*, 2012, **22**, 3634–3640.
- 26 Z. F. Li, C. Bommier, Z. S. Chong, Z. L. Jian, T. W. Surta, X. F. Wang, Z. Y. Xing, J. C. Neuefeind, W. F. Stickle, M. Dolgos, P. A. Greaney and X. L. Ji, *Adv. Energy Mater.*, 2017, **7**, 1602894.
- 27 T. Zhai, X. Lu, Y. Ling, M. Yu, G. Wang, T. Liu, C. Liang, Y. Tong and Y. Li, *Adv. Mater.*, 2014, **26**, 5869.
- 28 Y. C. Wang, T. Zhou, K. Jiang, P. M. Da, Z. Peng, J. Tang, B. Kong, W. B. Cai, Z. Q. Yang and G. F. Zheng, *Adv. Energy Mater.*, 2014, **4**, 1400696.
- 29 Y. W. Liu, H. Cheng, M. J. Lyu, S. J. Fan, Q. H. Liu, W. S. Zhang, Y. D. Zhi, C. M. Wang, C. Xiao, S. Q. Wei, B. J. Ye and Y. Xie, *J. Am. Chem. Soc.*, 2014, **136**, 15670–15675.
- 30 L. Qie, W. M. Chen, Z. H. Wang, Q. G. Shao, X. Li, L. X. Yuan, X. L. Hu, W. X. Zhang and Y. H. Huang, *Adv. Mater.*, 2012, **24**, 2047.
- 31 K. Rui, Z. Y. Wen, Y. Lu, J. Jin and C. Shen, *Adv. Energy Mater.*, 2015, **5**, 1401716.
- 32 D. F. Ying, R. Ding, Y. F. Huang, W. Shi, Q. L. Xu, C. N. Tan, X. J. Sun, P. Gao and E. H. Liu, *J. Mater. Chem. A*, 2019, **7**, 18257–18266.
- 33 P. Balaya, H. Li, L. Kienle and J. Maier, *Adv. Funct. Mater.*, 2003, **13**, 621–625.
- 34 H. Li, G. Richter and J. Maier, *Adv. Mater.*, 2003, **15**, 736–739.
- 35 S. Grugeon, S. Laruelle, R. Herrera-Urbina, L. Dupont, P. Poizot and J.-M. Tarascon, *J. Electrochem. Soc.*, 2001, **148**, A285–A292.
- 36 J. Wang, J. Polleux, J. Lim and B. Dunn, *J. Phys. Chem. C*, 2007, **111**, 14925–14931.
- 37 V. K. Mariappan, K. Krishnamoorthy, P. Pazhamalai, S. Sahoo, S. S. Nardekar and S.-J. Kim, *Nano Energy*, 2019, **57**, 307–316.
- 38 Q. L. Xu, R. Ding, W. Shi, D. F. Ying, Y. F. Huang, T. Yan, P. Gao, X. J. Sun and E. H. Liu, *J. Mater. Chem. A*, 2019, **7**, 8315–8326.
- 39 W. Shi, R. Ding, Q. L. Xu, T. Yan, Y. X. Huang, C. N. Tan, X. J. Sun, P. Gao and E. H. Liu, *Chem. Commun.*, 2019, **55**, 6739–6742.

